

Solid-State Gelation for Nanostructured Perovskite Oxide Aerogels

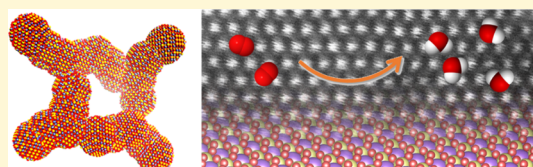
Bin Cai,^{†,‡,§} Karthik Akkiraju,^{§,||} William P. Mounfield, III,^{‡,||} Zhenshu Wang,[‡] Xing Li,[#] Botao Huang,^{†,§} Shuai Yuan,^{†,‡,§} Dong Su,[#] Yuriy Román-Leshkov,^{*,‡,||} and Yang Shao-Horn^{†,§,||,⊥}

[†]Research Laboratory of Electronics, [‡]Department of Chemical Engineering, [§]Electrochemical Energy Laboratory, ^{||}Department of Materials Science and Engineering, and [⊥]Department of Mechanical Engineering, Massachusetts Institute of Technology, Cambridge, Massachusetts 02139, United States

[#]Center for Functional Nanomaterials, Brookhaven National Laboratory, Upton, New York 11953, United States

Supporting Information

ABSTRACT: Fabricating nanostructured perovskite oxide aerogel to access a dramatic increase in the specific surface area has proved challenging despite continued efforts. Here, we report a versatile and general method for synthesizing nanosized perovskite oxides. Specifically, we used bimetallic “LaMnO_x” oxide nanoparticles as the precursors to synthesize r-LaMnO_{3±δ} perovskite oxide aerogels by way of a solid-state gelation process, generating aerogels with specific surface areas exceeding 74.2 m² g_{oxide}⁻¹. The r-LaMnO_{3±δ} aerogel featured an increased Mn valence state compared to the bulk form of the material, facilitating the oxygen reduction reaction kinetics in alkaline medium. At 0.8 V_{RHE}, the r-LaMnO_{3±δ} aerogel achieved a mass activity of 66.2 A g_{oxide}⁻¹, which is 153-fold higher mass activity compared to the conventional bulk LaMnO₃. The solid-state gelation synthesis route was extended to other perovskite oxides with high compositional diversity, including LaMnO₃, LaFeO₃, LaNiO₃, LaCoO₃, La_{0.5}Sr_{0.5}CoO₃, and La_{0.5}Sr_{0.5}Co_{0.5}Fe_{0.5}O₃, thereby demonstrating the versatile nature of our synthetic route for the fabrication of a wide range of nanostructured perovskite oxides.



Perovskite oxides, with the general formula of ABO₃, have been widely used as catalytic,¹ photovoltaic,² superconductive,³ and ferroelectric materials,⁴ because of their exceptional physical properties including electronic structure,⁵ ionic conductivity,⁶ electron mobility,⁷ and structural stability.⁸ The B-site cations in the crystal structure are typically 3d, 4d, or 5d transition-metal cations that are 6-fold coordinated with oxygen, resulting in octahedrons sharing corners in a cubic array. The A-site cations are generally large rare-earth, alkaline-earth, and alkali cations, which fill in the dodecahedral interstices. The large variety of A/B cations and the flexible substitution by foreign cations with different oxidation states impart highly tunable physicochemical properties upon perovskite oxides.^{9–13} The general synthesis of perovskite oxides is conducted by annealing the stoichiometric mixture of metal oxides or blended metal salts. High temperatures (above 900 °C) and long calcination times (more than 12 h) are often required to homogenize and re-arrange the A/B site atoms into a perovskite structure.¹⁴ These conditions result in significant particle agglomeration and low specific surface areas (below 1 m² g_{oxide}⁻¹), which are not ideal for catalysis applications.^{14–16}

Accordingly, over the last decade, the development of methods such as flame spray pyrolysis,¹⁷ porous silica templating,¹⁸ hydrothermal precipitation coupled with calcination,¹⁹ and laser ablation,²⁰ have emerged to prepare perovskite oxides with high specific surface area. For select cation combinations, these methods have produced perovskite oxides with the particle sizes ranging from 5 to 15 nm.^{17,21}

However, extending these techniques to other combinations typically results in decreased crystallinity,²² which stands in stark contrast to the general synthesis methods used for other nanostructured heterometallic oxides, such as spinels, through simple wet-chemical methods.²³ Therefore, new synthetic strategies toward controllable particle size, higher catalytic efficiency, and reduced synthetic cost are needed for the use of perovskite oxides in practical catalytic applications.²⁴

As synthetic porous solids, aerogels have demonstrated great potential as unsupported electrocatalysts owing to their outstanding features, such as low density, highly continuous porosity, and large specific surface areas.²⁵ Assembled from colloidal nanoparticles (NPs), aerogels can inherit the properties and functions from the nanoscale while maintaining macroscale aerogel properties.^{26–29} Transition-metal oxide aerogels have been reported for many elements, including yttrium,³⁰ tungsten,³¹ titanium³² and copper,³³ through sol-gel synthesis routes. Indeed, fabricating perovskite oxides with an aerogel structure would maximize active site utilization and provide the surface property advantages of nanostructured materials, while maintaining a robust macroscopic architecture.^{34,35} However, the typical gelation processes in oxide aerogel synthesis are mediated by solvent interactions under mild conditions, which would not be easily translatable to the

Received: August 7, 2019

Revised: October 10, 2019

Published: October 10, 2019

high temperature conditions required to homogenize and crystallize the lattice-mismatched AO_x and BO_x into a perovskite structure.

Here, we demonstrate a general solid-state gelation method combining multiple process (i.e., controlled elimination of solvent and crystallization of bimetallic oxides) using carbon as the solvent to generate perovskite oxide aerogels. We selected LaMnO_3 , one of the most active perovskite oxides for oxygen reduction reaction (ORR), as the target for our nanostructuring studies.¹⁶ First, bimetallic oxide “ LaMnO_x ” NPs were synthesized via a seed-mediated growth method and used as precursors for the perovskite oxide nanostructures. Next, a solid-state dispersion of the precursor NPs was obtained by deposition of “ LaMnO_x ” NPs onto a porous carbon matrix, which was considered as the solid “sol”. The solid-state gelation process was performed by accelerated calcination of the “sol” in air at high temperatures, during which the “solvent” (i.e., carbon) was evaporated (i.e., burned) and the precursor NPs formed an interconnected 3D perovskite aerogel structure. Decreasing the size of the perovskite into the nanoscale regime caused an increase in the Mn valence, thereby leading to increased activity for ORR. Specifically, when comparing the current density at 0.8 V_{RHE} , the $\text{LaMnO}_{3\pm\delta}$ aerogels exhibited a 153-fold higher mass activity than the bulk material. Importantly, the solid-state gelation method can be extended to other perovskite oxide compositions, such as Co-based perovskite oxide aerogels, which exhibited largely increased mass activity for the oxygen evolution reaction (OER).

RESULTS AND DISCUSSION

Synthesis of “ LaMnO_x ” Precursor NPs. We used a seed-mediated growth method to synthesize “ LaMnO_x ” NPs, as shown in Figure 1. This method side-stepped the co-nuclei

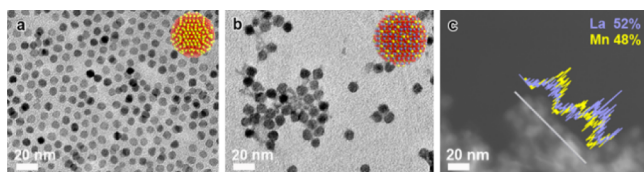


Figure 1. Seed-mediated growth synthesis of “ LaMnO_x ” precursor NPs. TEM images of (a) Mn_3O_4 seed NPs and (b) “ LaMnO_x ” NPs. (c) TEM–EDX line scan profile along with the indicated gray line. The “ LaMnO_x ” precursor NPs were synthesized by decomposing $\text{La}(\text{acac})_3$ in the presence of Mn_3O_4 seed NPs in oleylamine at 230 °C.

formation step and suppressed phase separation,³⁶ as La–O and Mn–O species are not considered generally to be miscible at the nanoscale due to the disparate atomic sizes of La/Mn and different reactivity of their precursors, thus hindering the design of homogeneous La–Mn–O nano-precursors (Figure S1). First, Mn_3O_4 seed NPs with a uniform diameter of ~ 8.2 nm were synthesized using oleylamine as capping agent (Figure 1b). Next, $\text{La}(\text{acac})_3$ was decomposed in the presence of Mn_3O_4 NPs in oleylamine at 230 °C to coat La–O species on the surface of Mn_3O_4 seeds. The resulting “ LaMnO_x ” precursor NPs remained well dispersed with a slightly increased diameter of ~ 9.5 nm (Figure 1c). The distributions of La and Mn across different NPs were reasonably homogeneous, having an atomic ratio of 1:1, as revealed by

the transmission electron microscopy energy-dispersive X-ray spectroscopy (TEM–EDX) line-scan analysis (Figure 1c).

Synthesis of $r\text{-LaMnO}_{3\pm\delta}$ Aerogel via Solid-State Gelation. We developed a novel solid-state gelation route by applying carbon as the dispersion medium for the synthesis of perovskite oxide aerogel. The gelation process that transform molecules in solution (sol) into a monolithic network (gel) by cross-linking has been widely used for the production of hydrogels and aerogels.³⁷ Similarly, preformed colloidal NPs dispersed in liquid medium have been shown to undergo a similar sol–gel process to form aerogels.²⁸ However, the requisite high temperature calcination hampers the application of such liquid-phase gelation in the design of perovskite oxide aerogels. In this work, we used porous carbon as a solid-state “solvent” to disperse the “ LaMnO_x ” precursor NPs, which is considered as the “sol” (Figure 2a). Instead of solvation in conventional liquid sol, the solid-state “sol” preserved the dispersion of “ LaMnO_x ” NPs by physically separating them by carbon support (Figure 2b). Next, we simulated the “gelation” process by performing an accelerated calcination at high temperature (800 °C) in air with a goal of facilitating the motion of the “ LaMnO_x ” NPs (Figure 2c). This calcination caused three beneficial effects: (i) as the carbon matrix was progressively burned, it facilitated the controlled fusion and connection of the NPs into an interconnected 3D gel structure; (ii) it promoted the formation of the perovskite structure by overcoming the high crystallization energy barrier; and (iii) it bypassed the solvent drying step needed in standard liquid-phase hydrogel syntheses to form the desired aerogels.

As shown in Figure 2d, the solid-state gelation resulted in a well-defined aerogel structure with a 3D network array composed of nanowires with an average diameter ranging from 10.1 to 14.6 nm. The diameter was further altered by tuning the temperature ramp rates (Figure S2). These nanowires fused and interconnected randomly during the elimination of solid solvent, resulting in a broad pore size distribution with open pores. The electron energy loss spectroscopy (EELS) elemental maps revealed the uniform distribution of La and Mn throughout the nanowire backbones (Figure 2e). As shown in Figure 2f, the high-resolution scanning TEM (HR-STEM) and corresponding fast Fourier transform (FFT) patterns demonstrated that the aerogel was highly crystalline, with rhombohedral perovskite structure and space group $R\bar{3}c$ (denoted as $r\text{-LaMnO}_{3\pm\delta}$ aerogel), which is in good agreement with X-ray powder diffraction (XRD) analysis (Figure S3a). The crystal size estimated from powder XRD by the Scherrer equation is 9.3 nm. The specific surface area of the $r\text{-LaMnO}_{3\pm\delta}$ aerogel sample was $74.2 \text{ m}^2 \text{ g}^{-1}$, as estimated by N_2 physisorption isotherm (Figure S3b), which corresponds to a ~ 100 -fold improvement over the typical bulk perovskite oxides.^{15,16}

The oxidation state of Mn in the $r\text{-LaMnO}_{3\pm\delta}$ aerogel was examined by X-ray photoelectron spectroscopy (XPS), EELS, and X-ray absorption near edge structure (XANES) analysis. As shown in Figure 3a, the $r\text{-LaMnO}_{3\pm\delta}$ aerogel featured a slightly smaller splitting (4.91 eV) than micron-sized $r\text{-LaMnO}_{3\pm\delta}$ particles (5.10 eV) for the doublet splitting of the Mn 3s core level, demonstrating Mn valence states of 3.46 and 3.32, respectively,^{38,39} which is in agreement with the analysis of the Mn 2p peaks (Figure S4a). EELS spectra collected on the scanning TEM showed that the ionization of electrons at Mn L_3 edge occurred at higher energy for $r\text{-LaMnO}_{3\pm\delta}$ aerogel than micron-sized $r\text{-LaMnO}_{3\pm\delta}$ particles as

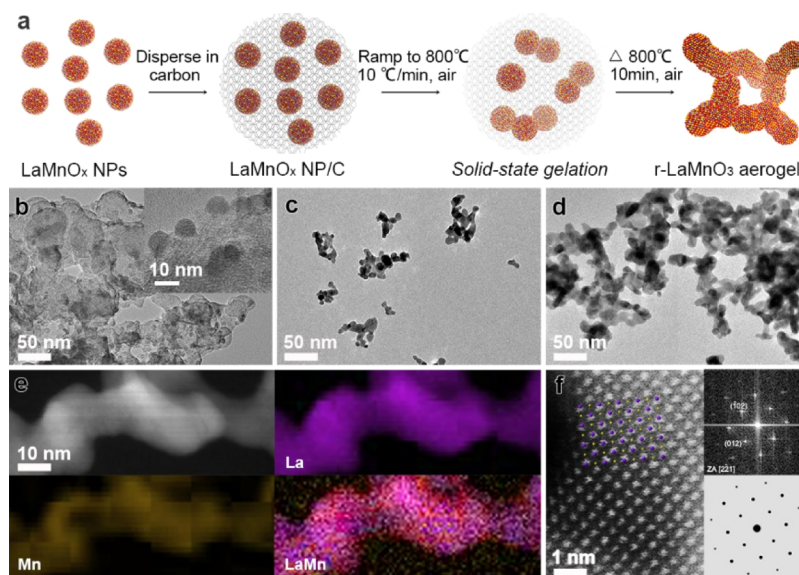


Figure 2. Solid-state gelation synthesis of $r\text{-LaMnO}_{3\pm\delta}$ aerogels. (a) Schematic illustration of the solid-state gelation mechanism transforming “ LaMnO_x ” NPs to $r\text{-LaMnO}_{3\pm\delta}$ aerogel. TEM images of (b) “ LaMnO_x ” NPs dispersed on porous carbon, (c) intermediate state during gelation, (d) $r\text{-LaMnO}_{3\pm\delta}$ perovskite oxide aerogel. (e) EELS elemental maps and (f) HR-STEM image of the $r\text{-LaMnO}_{3\pm\delta}$ aerogel backbone. Insets in (f) are corresponding FFT pattern (up) and simulated diffraction pattern (down) views along the $[2-21]$ zone axis. The solid-state gelation for $r\text{-LaMnO}_{3\pm\delta}$ aerogels was initiated at 800°C for 10 min in air.

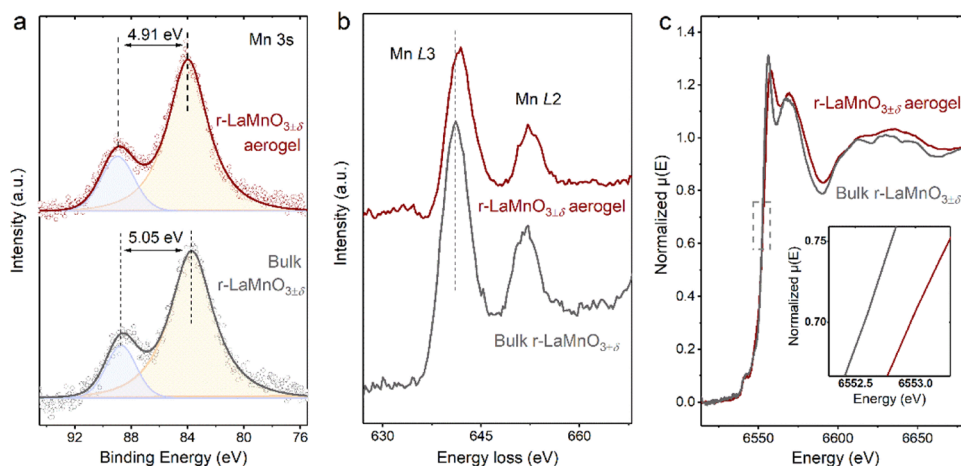


Figure 3. Study of the Mn valence state of $r\text{-LaMnO}_{3\pm\delta}$ aerogel. (a) XPS Mn 3s peak, (b) EELS of Mn L edge and (c) XANES of Mn K edge of both aerogel and bulk forms of $r\text{-LaMnO}_{3\pm\delta}$ perovskite showing the increased Mn valence for $r\text{-LaMnO}_{3\pm\delta}$ aerogel. The inset of (c) shows zoomed-in plots from the dashed square. The EELS measurement was performed by exposing the material under a focused electron beam and collect signals from the electron beam illuminated area.

well as the higher intensity ratio of L_3/L_2 for the $r\text{-LaMnO}_{3\pm\delta}$ aerogel,⁴⁰ further supporting higher Mn valence state for the aerogel (Figure 3b).⁴¹ Figure 3c shows the normalized XANES spectra at the Mn K-edge. A chemical shift of the pre-edge feature of the $r\text{-LaMnO}_{3\pm\delta}$ aerogel with respect to bulk material provides further evidence for the increasing Mn valence, which was further demonstrated in the derivative spectrum (Figure S4b). By comparing the pre-edge position with standard Mn_2O_3 and MnO_2 , the Mn valence states are 3.53 and 3.43 for $r\text{-LaMnO}_{3\pm\delta}$ aerogel and micron-sized $r\text{-LaMnO}_{3\pm\delta}$ particles, respectively (Figure S4d,e).⁴²

To obtain more structural information, ex situ extended X-ray absorption fine structure (EXAFS) spectra were obtained. Figure S4c shows the k^2 weighted Mn K-edge EXAFS spectra for both $r\text{-LaMnO}_{3\pm\delta}$ aerogel and micron-sized $r\text{-LaMnO}_{3\pm\delta}$. The dominant peak at $\sim 1.4 \text{ \AA}$ is assigned to the first

shell coordination of Mn–O, while the relatively weak peak at 3.0 is associated with the second shell comprising a combination of Mn–La, Mn–Mn single, and Mn–O multiple scattering paths. The least square fit gives an average Mn–O bond length of 1.98 \AA for $r\text{-LaMnO}_{3\pm\delta}$ aerogel and 2.02 \AA for micron-sized $r\text{-LaMnO}_{3\pm\delta}$, which is in agreement with previous LaMnO_3 perovskites (Table S1).⁴³

Transformation of “ LaMnO_x ” Precursor NPs to $o\text{-LaMnO}_{3\pm\delta}$ Perovskite NPs. The “ LaMnO_x ” NPs that contain both La and Mn were crystallized into the perovskite structure when exposed to elevated temperature in an inert atmosphere (Figure 4a). The resulting $\text{LaMnO}_{3\pm\delta}$ perovskite NPs ranged from 10 to 40 nm in diameter (Figure 4b). The nonuniformity of particle sizes could be ascribed to the mobility of the NPs during calcination, and resulting in sintering of adjacent NPs. Figure 4c shows the EELS elemental maps, confirming the

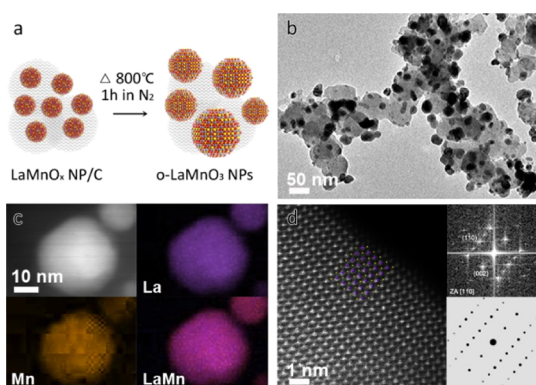


Figure 4. Transformation of “LaMnO_x” NPs to o-LaMnO_{3±δ} perovskite oxide NPs. (a) Scheme of the crystallization of “LaMnO_x” NPs to o-LaMnO_{3±δ} perovskite oxide NPs at 800 °C in a N₂ atmosphere. (b) TEM image, (c) EELS elemental maps and (d) HR-STEM image of the o-LaMnO_{3±δ} perovskite oxide NPs. Insets in (d) are corresponding FFT pattern (up) and simulated diffraction pattern (down) views along the [110] zone axis.

homogeneous distribution of A/B-site atoms within individual NPs. XRD analysis confirmed an orthorhombic structure with a space group of *Pnma* (Figure S5a), thus denoted as o-LaMnO_{3±δ} NPs. The HR-STEM and corresponding FFT pattern further confirmed the *Pnma* structure of the o-LaMnO_{3±δ} NPs (Figure 4d).

Electrocatalytic Activity for ORR. The electrocatalytic ORR activity was evaluated by cyclic voltammetry (CV) using a thin film of oxides supported on the glassy carbon electrode (GCE) in O₂-saturated 0.1 M KOH at a rotation speed of 1600 rpm.⁴⁴ To prevent electroreduction of the oxide catalysts, the CVs were conducted in the potential range of 0.72–1.05 V_{RHE}. The r-LaMnO_{3±δ} aerogel was found to have the onset of the ORR at 0.9 V_{RHE} similar to Pt/C and much higher than o-LaMnO_{3±δ} NPs and micron-sized r-LaMnO_{3±δ} (Figure 5a). The onset potential does not necessarily correlate with intrinsic or mass activity as it is influenced by the catalyst loading and surface area in addition to intrinsic or specific activity.⁴⁵ The kinetic current densities obtained from the polarization curves were normalized by either surface areas or mass of the oxide or Pt, generating the specific activities and mass activities. Figure 5b,c shows the resulting Tafel plots for the r-LaMnO_{3±δ} aerogel and the o-LaMnO_{3±δ} NPs in comparison with the micron-sized LaMnO_{3±δ} and commercial Pt/C (TKK, 46.6 wt %). The r-LaMnO_{3±δ} aerogel shows comparable specific activity compared to the micron-sized r-LaMnO_{3±δ} measured in this work and previous work.^{46,47} Remarkably, the r-LaMnO_{3±δ} aerogel showed a mass activity of 66.2 A g_{oxide}⁻¹ at 0.8 V_{RHE}, which is ~150-fold higher than that of the micron-sized LaMnO_{3±δ} (Figure 5c). The mass activity maintained across different catalyst loading on GCE (Figure S6). To the best of our knowledge, this is the highest value reported upon perovskite oxides.²⁴ While the o-LaMnO_{3±δ} NPs had lower specific activity, its mass activity shows a 5-fold improvement over the micron-sized r-LaMnO_{3±δ}.

The ORR kinetics of the r-LaMnO_{3±δ} aerogels was further examined by collecting the polarization curves at different rotation speeds (Figure S7). Based on the slope of the Koutecky–Levich plot, the electron transfer number (*n*) was calculated to be 4.0, indicating a complete reduction of oxygen. In addition, no H₂O₂ was detected from the RRDE test during the ORR. Besides the improved activity, the r-LaMnO_{3±δ}

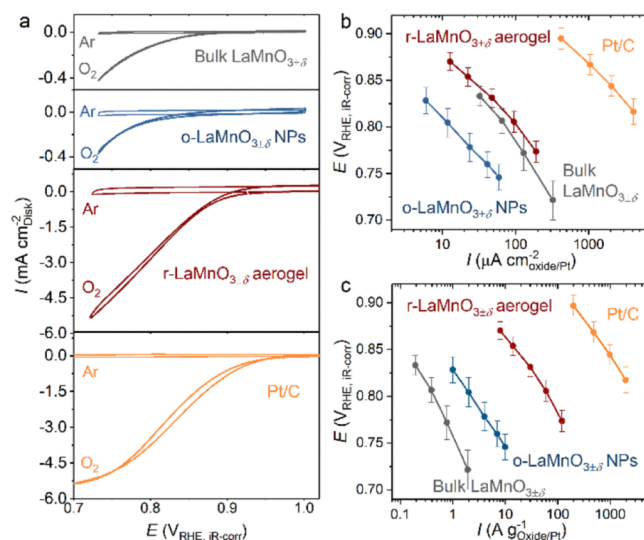


Figure 5. ORR performance of LaMnO_{3±δ} NPs and aerogels. (a) CV measurements from Ar- and O₂-saturated 0.1 M KOH recorded at 10 mV s⁻¹ in comparison with TKK Pt/C (46.6 wt %) and micron-sized LaMnO_{3±δ} with a rotation speed of 1600 rpm. Comparisons of (b) mass activity and (c) specific activity of the LaMnO_{3±δ} perovskites (both nanosized and bulk forms) and TKK Pt/C. Background current and *i*R drop were corrected for activity calculations. Specific activity was obtained by normalizing current by the BET surface area of oxides or ECSA of Pt. Acid treated acetylene black (AB) was applied for perovskite catalysts. The final compositions for the electrodes were 250 μg_{oxide} cm_{disk}⁻², 50 μg_{AB} cm_{disk}⁻² for bulk LaMnO_{3±δ} and r-LaMnO_{3±δ} aerogel; 30 μg_{oxide} cm_{disk}⁻², 70 μg_{carbon} cm_{disk}⁻² for o-LaMnO_{3±δ} NPs, and 10 μg_{Pt} cm_{disk}⁻² for Pt/C. Nafion loading is 50 μg cm_{disk}⁻² for all measurements. Error bars were obtained from standard deviation based on at least three independent measurements.

aerogel structure also demonstrates excellent durability as indicated by chronoamperometric measurements. As shown in Figure S8, nearly 90% of the current density was maintained after 5 h of continuous operation at 0.77 V_{RHE}.

Versatility of the Solid-State Gelation for Perovskite Oxide Nanostructures. Because the gelation of precursor NPs is based on the welding between adjacent NPs which includes atom exchange between them, here, the solid-state gelation strategy offers a possibility to use separated AO_x and BO_x NPs as the precursor for the synthesis of ABO₃ aerogels. To verify this, instead of “LaMnO_x” NPs, easily obtainable monometallic oxide (i.e., LaO_x and MnO_x) NPs were mixed as precursors and perovskite LaMnO_{3±δ} aerogel with an average diameter of 17 nm was obtained through solid-state gelation of mixed La₂O₃ and Mn₃O₄ NPs (Figure S9). Similarly, LaFeO₃ aerogel was also synthesized using mixed La₂O₃ and Fe₃O₄ NPs as precursors (Figure S9). The solid-state gelation method shows two advantages compared to traditional sol–gel synthesis in liquid media: (i) it is suitable for high temperatures and (ii) further drying step is eliminated because of the combustion of dispersing media (i.e., carbon) after ~2 h, demonstrating excellent stability of La_{0.5}Sr_{0.5}Co_{0.5}Fe_{0.5}O₃ aerogel (Figure S12).

To make this strategy more versatile, the precursor options for solid-state gelation were extended to molecules (i.e., metal salts), thus making the strategy applicable to virtually any perovskite oxide formulation. We demonstrate the applicability of the method herein through the synthesis of perovskite oxide aerogels with composition of LaMnO₃, LaFeO₃, LaNiO₃,

LaCoO₃, La_{0.5}Sr_{0.5}CoO₃, and La_{0.5}Sr_{0.5}Co_{0.5}Fe_{0.5}O₃ based on corresponding metal nitrates as precursor. The TEM images (Figure 6) demonstrate the well-defined aerogel network

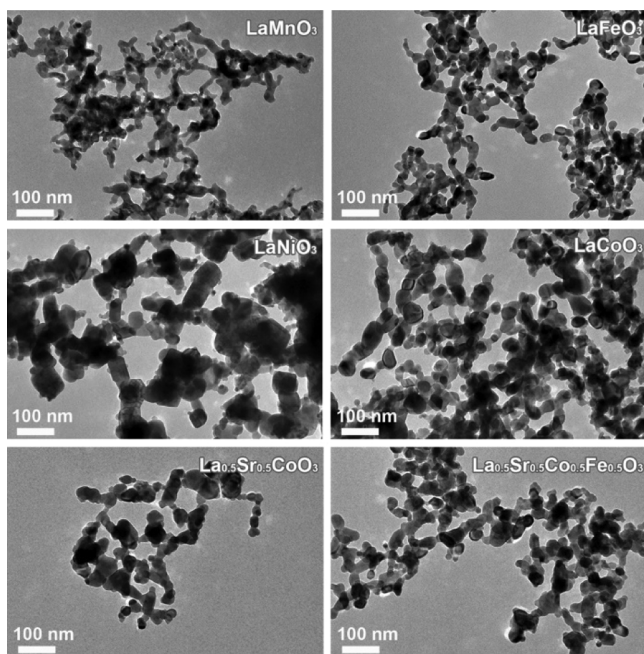


Figure 6. Versatility of the solid-state gelation strategy using molecular precursors. TEM images of nanostructured perovskite oxide aerogels with compositions of LaMnO₃, LaFeO₃, LaNiO₃, LaCoO₃, La_{0.5}Sr_{0.5}CoO₃, and La_{0.5}Sr_{0.5}Co_{0.5}Fe_{0.5}O₃.

structure and high porosity of the as-synthesized aerogels. Their perovskite structures were confirmed by XRD analysis (Figure S10). Using OER as a probe reaction, the Co-based perovskites show a clear materials design roadmap with gradually increased mass activities (current density at 1.6 V_{RHE}) of LaCoO₃, La_{0.5}Sr_{0.5}CoO₃, and La_{0.5}Sr_{0.5}Co_{0.5}Fe_{0.5}O₃ aerogels by factors of ~13.8, ~43.6, and ~145.3 compared with micron-sized LaCoO₃ (Figure S11). The mass activity of La_{0.5}Sr_{0.5}Co_{0.5}Fe_{0.5}O₃ aerogel is comparable to one of the most active flame-synthesized Ba_{0.5}Sr_{0.5}Co_{0.5}Fe_{0.5}O₃ nanopowder (16 A g_{metal}⁻¹ at 1.55 V_{RHE})¹⁷ and much higher than most of the micron-sized perovskite oxides (<2 A g_{oxide}⁻¹ at 1.55 V_{RHE}).¹⁵ The specific activity of La_{0.5}Sr_{0.5}Co_{0.5}Fe_{0.5}O₃ aerogel at 1.55 V_{RHE} is 0.05 mA cm_{oxide}⁻², which is in the range of the Co-based perovskite oxide powders).¹⁵ Furthermore, the galvanostatic measurement shows no obvious change of overpotential.

CONCLUSIONS

In summary, we have developed a unique and versatile solid-state gelation strategy for the design of perovskite oxide aerogel nanostructures with both large surface area and high crystallinity. In the meantime, nearly monodisperse bimetallic oxide “LaMnO_x” NPs were developed through a seed-growth method. Using that as the precursor, we synthesized LaMnO_{3±δ} perovskite oxide aerogels by way of a solid-state gelation process, generating aerogels with specific surface areas exceeding 74.2 m² g_{oxide}⁻¹. Perovskite oxide o-LaMnO_{3±δ} NPs were fabricated by facile calcination of the “LaMnO_x” NPs. The r-LaMnO_{3±δ} aerogel has an increased Mn valence state compared with the bulk form, which promotes ORR kinetics in

alkaline solution. As a result, the as-prepared r-LaMnO_{3±δ} aerogel achieved a mass activity of 66.2 A g_{oxide}⁻¹ at 0.8 V_{RHE}, which is ~150-fold higher than the bulk material. In addition, the solid-state gelation was further extended to perovskite oxides with other compositions, resulting in largely increased OER mass activity for Co-based perovskite oxide aerogels. This work demonstrates a versatile synthetic route for the fabrication of nanostructured perovskite oxides and opens up the door to many other possibilities for different applications.

METHODOLOGY

Synthesis of “LaMnO_x” Precursor NPs. The Mn₃O₄ seed was synthesized according to a reported procedure. Briefly, 0.17 g manganese(II) acetate (1 mmol), 0.953 mL oleic acid (3 mmol), and 2.97 mL oleylamine (9 mmol) were dissolved in 15 mL xylene under stirring in an air atmosphere. The solution was slowly heated to 90 °C, and then 1 mL water was injected into the solution under vigorous stirring. The resulting solution was aged at 90 °C for 3 h. The resulting Mn₃O₄ NPs were precipitated using centrifugation by adding 20 mL ethanol and then further washed by hexanes/ethanol for 3 times. The final product was dispersed in 8 mL hexanes.

The “LaMnO_x” NPs were synthesized via a seed-mediated growth method using Mn₃O₄ NPs as the seed. In a typical synthesis, 220.5 mg lanthanum(III) acetylacetonate (0.5 mmol) was dissolved in 15 mL oleylamine and heated to 110 °C under nitrogen flow to remove dissolved oxygen and moisture. Then, 3.2 mL Mn₃O₄ solution (0.4 mmol Mn) was injected into the solution under nitrogen protection. The solution was kept stirring at 110 °C for 40 min to fully evaporate hexanes. Then, the solution was heated to 260 °C at 5 °C min⁻¹ and aged for 3 h. The resulting “LaMnO_x” NPs were precipitated out by addition of 20 mL ethanol and then further washed by hexanes/ethanol for 3 times. The final product was dispersed in 20 mL hexanes.

Solid-State Gelation for r-LaMnO_{3±δ} Aerogels. The solid sol was prepared by dispersing corresponding precursor NPs in carbon black. Specifically, the afore-mentioned “LaMnO_x” NP dispersion was firstly diluted to 0.5 mg mL⁻¹ in hexane and isopropanol (v/v 2:1). A certain amount of carbon black was dispersed in hexane and isopropanol (v/v 2:1) via sonication for 30 min. The precursor NP dispersion and carbon dispersion were mixed to obtain a weight ratio of 1:2 (oxide/carbon), followed by sonication for 2 h. The “LaMnO_x” NP/C was separated by centrifuge and dried under vacuum. The solid-state gelation was performed using a controlled calcination process in air. A ceramic crucible was used to carry the LaMnO_x/C, then the temperature was ramped to 800 °C at 10 °C min⁻¹ and aged for 10 min under air flow of 100 mL min⁻¹. To adjust the diameter, the ramping rate can be tuned from 5 to 20 °C min⁻¹. The precursor NPs can be replaced by a mixture of A-site and B-site oxide NPs, while the other steps remaining the same. The generalization of solid-state gelation to other compositions was using metal nitrites as the metal precursor by impregnation of the stoichiometric amount of metal salts in carbon black, while the gelation step remaining the same.

Synthesis of o-LaMnO_{3±δ} NPs and Bulk Materials. “LaMnO_x” NP solution (10 mL, about 50 mg) was diluted to 70 mL by adding a 60 mL mixture of hexanes/isopropanol (1:1 vol) and sonication for 30 min. Carbon black (150 mg) was dispersed in 150 mL hexane/isopropanol (1:1 vol) by sonication for 30 min. The diluted “LaMnO_x” NP solution

was mixed with the carbon black dispersion, followed by sonication for 2 h. The LaMnO_x/C was precipitated by centrifugation and dried under vacuum. For the synthesis of $\text{o-LaMnO}_{3\pm\delta}$ NPs, the LaMnO_x/C was subjected to a calcination at 800°C for 1 h under nitrogen flow with a ramping rate of 2°C min^{-1} . The bulk $\text{r-LaMnO}_{3\pm\delta}$ perovskite oxide was synthesized at 800°C for 24 h in air.¹⁶

Electrochemical Measurements. The Nafion solution was ion-exchanged by adding 0.1 mL 0.1 M KOH to 0.2 mL Nafion solution (5 wt %). Catalyst ink of aerogel was prepared by sonication of 4 mg oxide aerogels, 1 mg acid-treated AB, 60 μL Nafion solution, and 1.94 mL mixture of water/isopropanol (v/v 1:1) for at least 1 h. Catalyst ink of $\text{o-LaMnO}_{3\pm\delta}$ NP/C was prepared by sonication of 2 mg $\text{o-LaMnO}_{3\pm\delta}$ NP/C, 60 μL Nafion solution, and 0.94 mL mixture of water/isopropanol (v/v 1:1) for at least 1 h. Catalyst ink of bulk perovskite oxide was prepared by sonication of 5 mg oxide, 1 mg acid-treated AB, 60 μL Nafion solution, and 0.94 mL mixture of water/isopropanol (v/v 1:1) for at least 1 h. Next, 10 μL of the catalyst inks was drop-casted onto pre-polished GCE (0.196 cm^2) and dried in an ambient atmosphere. The catalyst loadings are $250 \mu\text{g}_{\text{oxide}} \text{cm}_{\text{disk}}^{-2}$ for $\text{r-LaMnO}_{3\pm\delta}$ aerogel and bulk $\text{LaMnO}_{3\pm\delta}$, $30 \mu\text{g}_{\text{oxide}} \text{cm}_{\text{disk}}^{-2}$ for $\text{o-LaMnO}_{3\pm\delta}$ NP/C. For comparison, the platinum electrode was prepared using commercial Pt/C catalyst (46 wt %, TKK) targeting a Pt loading of $10 \mu\text{g}_{\text{oxide}} \text{cm}_{\text{disk}}^{-2}$. Specific activity was obtained by normalizing the kinetic current with the surface area that was estimated from N_2 physisorption. All measurements were conducted at 10 mV s^{-1} in either Ar or O_2 (ultrahigh purity grade, Airgas) saturated 0.1 M KOH, which was prepared from Milli-Q water ($18.2 \text{ M}\Omega \text{ cm}^{-1}$) and KOH pellets (99.99 wt %). A Hg/HgO electrode was used as the reference electrode and calibrated by measuring hydrogen oxidation/evolution currents on Pt-electrode and defining the potential of zero current as 0 V_{RHE} . The uncompensated Ohmic electrolyte resistance ($\approx 45 \Omega$) measured via high frequency ac impedance in O_2 -saturated 0.1 M KOH. ORR activities were obtained from the negative-going scans in pure O_2 at 1600 rpm and were corrected for capacitive currents. Error bars represent standard deviations from at least three independent repeated measurements.

Apparatus and Characterizations. XRD was carried out with a Bruker D8-Focus Bragg–Brentano X-ray powder diffractometer equipped with a Cu sealed tube ($\lambda = 1.54178 \text{ \AA}$) at 40 kV and 40 mA. TEM measurements were conducted on a FEI Tecnai G2 F20 ST microscope operated at 120 kV. TEM–EDX analysis was performed on a JEOL 2010F microscope operated at 200 kV. High-angle annular dark-field-STEM and EELS were performed using a Hitachi HD2700C (200 kV) equipped with a probe aberration corrector at Brookhaven National Laboratory. Specific surface areas were calculated based on the nitrogen adsorption and desorption isotherms that were measured on a Quantachrome Autosorb iQ apparatus, applying the Brunauer–Emmett–Teller (BET) equation. XPS was performed with a Thermo Scientific K-Alpha ESCA spectrometer, using monochromatic Al $K\alpha$ radiation (1486.6 eV) and a low energy flood gun as a neutralizer. The binding energy of the C 1s peak at 284.6 eV was used as a reference. Ex situ XAS measurements on the Ni K-edge were carried out at Beamline 8-ID, National Synchrotron Light Source II, Brookhaven National Laboratory, using a Si(111) monochromator and a Lytle detector. The valence state of Mn was probed based on the K pre-edge energy position.

■ ASSOCIATED CONTENT

Supporting Information

The Supporting Information is available free of charge on the ACS Publications website at DOI: [10.1021/acs.chemmater.9b03182](https://doi.org/10.1021/acs.chemmater.9b03182).

TEM images of phase separated La–Mn–O; N_2 physisorption; ORR measurement with varied catalyst loading and rotation speed; stability test; Mn 2p XPS spectra; EXAFS analysis; density functional theory calculated lattice strained perovskite; TEM images of solid-state gelation from mixed oxide NPs; and OER performance of Co-based perovskite oxide aerogels (PDF).

■ AUTHOR INFORMATION

Corresponding Author

*E-mail: yroman@mit.edu.

ORCID

Bin Cai: 0000-0002-3263-0395

William P. Mounfield, III: 0000-0003-0770-3297

Botao Huang: 0000-0001-5634-5620

Shuai Yuan: 0000-0003-3329-0481

Dong Su: 0000-0002-1921-6683

Yuriy Román-Leshkov: 0000-0002-0025-4233

Yang Shao-Horn: 0000-0001-8714-2121

Notes

The authors declare no competing financial interest.

■ ACKNOWLEDGMENTS

This work was supported by the Toyota Research Institute through the Accelerated Materials Design and Discovery program. This research used beamline 8-ID (ISS) of the National Synchrotron Light Source II, and the Center for Functional Nanomaterials, U.S. Department of Energy (DOE) Office of Science User Facilities operated for the DOE Office of Science by Brookhaven National Laboratory under contract no. DE-SC0012704.

■ REFERENCES

- (1) Hwang, J.; Rao, R. R.; Giordano, L.; Katayama, Y.; Yu, Y.; Shao-Horn, Y. Perovskites in catalysis and electrocatalysis. *Science* **2017**, *358*, 751–756.
- (2) Yang, S. Y.; Seidel, J.; Byrnes, S. J.; Shafer, P.; Yang, C.-H.; Rossell, M. D.; Yu, P.; Chu, Y.-H.; Scott, J. F.; Ager, J. W., III; Martin, L. W.; Ramesh, R. Above-bandgap voltages from ferroelectric photovoltaic devices. *Nat. Nanotechnol.* **2010**, *5*, 143–147.
- (3) Oudah, M.; Ikeda, A.; Hausmann, J. N.; Yonezawa, S.; Fukumoto, T.; Kobayashi, S.; Sato, M.; Maeno, Y. Superconductivity in the antiperovskite Dirac-metal oxide $\text{Sr}_{3-x}\text{SnO}$. *Nat. Commun.* **2016**, *7*, 13617.
- (4) Li, W.; Ji, L.-J. Perovskite ferroelectrics go metal free. *Science* **2018**, *361*, 132.
- (5) Lu, Q.; Chen, Y.; Bluhm, H.; Yildiz, B. Electronic Structure Evolution of SrCoO_x during Electrochemically Driven Phase Transition Probed by in Situ X-ray Spectroscopy. *J. Phys. Chem. C* **2016**, *120*, 24148–24157.
- (6) Navickas, E.; Chen, Y.; Lu, Q.; Wallisch, W.; Huber, T. M.; Bernardi, J.; Stöger-Pollach, M.; Friedbacher, G.; Hutter, H.; Yildiz, B.; Fleig, J. Dislocations Accelerate Oxygen Ion Diffusion in $\text{La}_{0.8}\text{Sr}_{0.2}\text{MnO}_3$ Epitaxial Thin Films. *ACS Nano* **2017**, *11*, 11475–11487.
- (7) Jeon, H.; Choi, W. S.; Biegalski, M. D.; Folkman, C. M.; Tung, I.-C.; Fong, D. D.; Freeland, J. W.; Shin, D.; Ohta, H.; Chisholm, M. F.;

Lee, H. N. Reversible redox reactions in an epitaxially stabilized SrCoO_x oxygen sponge. *Nat. Mater.* **2013**, *12*, 1057–1063.

(8) Mefford, J. T.; Hardin, W. G.; Dai, S.; Johnston, K. P.; Stevenson, K. J. Anion charge storage through oxygen intercalation in LaMnO₃ perovskite pseudocapacitor electrodes. *Nat. Mater.* **2014**, *13*, 726–732.

(9) Yin, W.-J.; Weng, B.; Ge, J.; Sun, Q.; Li, Z.; Yan, Y. Oxide perovskites, double perovskites and derivatives for electrocatalysis, photocatalysis, and photovoltaics. *Energy Environ. Sci.* **2019**, *12*, 442–462.

(10) Chen, G.; Zhou, W.; Guan, D.; Sunarso, J.; Zhu, Y.; Hu, X.; Zhang, W.; Shao, Z. Two orders of magnitude enhancement in oxygen evolution reactivity on amorphous Ba_{0.5}Sr_{0.5}Co_{0.8}Fe_{0.2}O_{3-δ} nanofilms with tunable oxidation state. *Sci. Adv.* **2017**, *3*, No. e1603206.

(11) Liu, R.; Liang, F.; Zhou, W.; Yang, Y.; Zhu, Z. Calcium-doped lanthanum nickelate layered perovskite and nickel oxide nano-hybrid for highly efficient water oxidation. *Nano Energy* **2015**, *12*, 115–122.

(12) Chen, G.; Zhu, Y.; Chen, H. M.; Hu, Z.; Hung, S. F.; Ma, N.; Dai, J.; Lin, H. J.; Chen, C. T.; Zhou, W.; Shao, Z. An Amorphous Nickel-Iron-Based Electrocatalyst with Unusual Local Structures for Ultrafast Oxygen Evolution Reaction. *Adv. Mater.* **2019**, *31*, No. e1900883.

(13) Shetty, M.; Zanchet, D.; Green, W. H.; Román-Leshkov, Y. Cooperative Co⁰/Co^{II} Sites Stabilized by a Perovskite Matrix Enable Selective C-O and C-C bond Hydrogenolysis of Oxygenated Arenes. *ChemSuschem* **2019**, *12*, 2171–2175.

(14) Royer, S.; Duprez, D.; Can, F.; Courtois, X.; Batiot-Dupeyrat, C.; Laassiri, S.; Alamdari, H. Perovskites as substitutes of noble metals for heterogeneous catalysis: dream or reality. *Chem. Rev.* **2014**, *114*, 10292–10368.

(15) Suntivich, J.; May, K. J.; Gasteiger, H. A.; Goodenough, J. B.; Shao-Horn, Y. A perovskite oxide optimized for oxygen evolution catalysis from molecular orbital principles. *Science* **2011**, *334*, 1383–1385.

(16) Suntivich, J.; Gasteiger, H. A.; Yabuuchi, N.; Nakanishi, H.; Goodenough, J. B.; Shao-Horn, Y. Design principles for oxygen-reduction activity on perovskite oxide catalysts for fuel cells and metal-air batteries. *Nat. Chem.* **2011**, *3*, 546–550.

(17) Fabbri, E.; Nachttegaal, M.; Binninger, T.; Cheng, X.; Kim, B.-J.; Durst, J.; Bozza, F.; Graule, T.; Schäublin, R.; Wiles, L.; Pertoso, M.; Danilovic, N.; Ayers, K. E.; Schmidt, T. J. Dynamic surface self-reconstruction is the key of highly active perovskite nano-electrocatalysts for water splitting. *Nat. Mater.* **2017**, *16*, 925–931.

(18) Nair, M. M.; Kaliaguine, S.; Kleitz, F. Nanocast LaNiO₃ Perovskites as Precursors for the Preparation of Coke-Resistant Dry Reforming Catalysts. *ACS Catal.* **2014**, *4*, 3837–3846.

(19) Wang, H.; Wang, J.; Pi, Y.; Shao, Q.; Tan, Y.; Huang, X. Double Perovskite LaFe_xNi_{1-x}O₃ Nanorods Enable Efficient Oxygen Evolution Electrocatalysis. *Angew. Chem., Int. Ed.* **2019**, *58*, 2316–2320.

(20) Kim, W. S.; Anoop, G.; Lee, H. J.; Lee, S. S.; Kwak, J. H.; Lee, H. J.; Jo, J. Y. Facile synthesis of perovskite LaMnO_{3+δ} nanoparticles for the oxygen reduction reaction. *J. Catal.* **2016**, *344*, 578–582.

(21) Kim, B.-J.; Cheng, X.; Abbott, D. F.; Fabbri, E.; Bozza, F.; Graule, T.; Castelli, I. E.; Wiles, L.; Danilovic, N.; Ayers, K. E.; Marzari, N.; Schmidt, T. J. Highly Active Nanoperovskite Catalysts for Oxygen Evolution Reaction: Insights into Activity and Stability of Ba_{0.5}Sr_{0.5}Co_{0.8}Fe_{0.2}O_{2+δ} and SrBaCo₂O_{5+δ}. *Adv. Funct. Mater.* **2018**, *28*, 1804355.

(22) Teoh, W. Y.; Amal, R.; Mädler, L. Flame spray pyrolysis: An enabling technology for nanoparticles design and fabrication. *Nanoscale* **2010**, *2*, 1324–1347.

(23) Zhao, Q.; Yan, Z.; Chen, C.; Chen, J. Spinels: Controlled Preparation, Oxygen Reduction/Evolution Reaction Application, and Beyond. *Chem. Rev.* **2017**, *117*, 10121–10211.

(24) Zhu, H.; Zhang, P.; Dai, S. Recent Advances of Lanthanum-Based Perovskite Oxides for Catalysis. *ACS Catal.* **2015**, *5*, 6370–6385.

(25) Cai, B.; Eychmüller, A. Promoting Electrocatalysis upon Aerogels. *Adv. Mater.* **2019**, *31*, No. e1804881.

(26) Mohanan, J. L.; Arachchige, I. U.; Brock, S. L. Porous semiconductor chalcogenide aerogels. *Science* **2005**, *307*, 397–400.

(27) Leventis, N. Three-dimensional core-shell superstructures: mechanically strong aerogels. *Acc. Chem. Res.* **2007**, *40*, 874–884.

(28) Cai, B.; Sayevich, V.; Gaponik, N.; Eychmüller, A. Emerging Hierarchical Aerogels: Self-Assembly of Metal and Semiconductor Nanocrystals. *Adv. Mater.* **2018**, *30*, 1707518.

(29) Zhu, C.; Shi, Q.; Fu, S.; Song, J.; Xia, H.; Du, D.; Lin, Y. Efficient Synthesis of MCu (M = Pd, Pt, and Au) Aerogels with Accelerated Gelation Kinetics and their High Electrocatalytic Activity. *Adv. Mater.* **2016**, *28*, 8779–8783.

(30) Cheng, W.; Rechberger, F.; Niederberger, M. Three-Dimensional Assembly of Yttrium Oxide Nanosheets into Luminescent Aerogel Monoliths with Outstanding Adsorption Properties. *ACS Nano* **2016**, *10*, 2467–2475.

(31) Cheng, W.; Rechberger, F.; Niederberger, M. From 1D to 3D - macroscopic nanowire aerogel monoliths. *Nanoscale* **2016**, *8*, 14074–14077.

(32) Heiligtag, F. J.; Cheng, W.; de Mendonça, V. R.; Süess, K.; Günther, D.; Ribeiro, C.; Niederberger, M.; Niederberger, M. Self-Assembly of Metal and Metal Oxide Nanoparticles and Nanowires into a Macroscopic Ternary Aerogel Monolith with Tailored Photocatalytic Properties. *Chem. Mater.* **2014**, *26*, 5576–5584.

(33) Ling, P.; Zhang, Q.; Cao, T.; Gao, F. Versatile Three-Dimensional Porous Cu@Cu₂O Aerogel Networks as Electrocatalysts and Mimicking Peroxidases. *Angew. Chem., Int. Ed.* **2018**, *57*, 6819–6824.

(34) Zhou, S.; Miao, X.; Zhao, X.; Ma, C.; Qiu, Y.; Hu, Z.; Zhao, J.; Shi, L.; Zeng, J. Engineering electrocatalytic activity in nanosized perovskite cobaltite through surface spin-state transition. *Nat. Commun.* **2016**, *7*, 11510.

(35) Zhao, Y.; Xu, L.; Mai, L.; Han, C.; An, Q.; Xu, X.; Liu, X.; Zhang, Q. Hierarchical mesoporous perovskite La_{0.5}Sr_{0.5}Co_{0.91} nanowires with ultrahigh capacity for Li-air batteries. *Proc. Natl. Acad. Sci. U.S.A.* **2012**, *109*, 19569–19574.

(36) Park, J.; Joo, J.; Kwon, S. G.; Jang, Y.; Hyeon, T. Synthesis of monodisperse spherical nanocrystals. *Angew. Chem., Int. Ed.* **2007**, *46*, 4630–4660.

(37) Pierre, A. C.; Pajonk, G. M. Chemistry of aerogels and their applications. *Chem. Rev.* **2002**, *102*, 4243–4266.

(38) Ilton, E. S.; Post, J. E.; Heaney, P. J.; Ling, F. T.; Kerisit, S. N. XPS determination of Mn oxidation states in Mn (hydr)oxides. *Appl. Surf. Sci.* **2016**, *366*, 475–485.

(39) Galakhov, V. R.; Demeter, M.; Bartkowski, S.; Neumann, M.; Ovechikina, N. A.; Kurmaev, E. Z.; Lobachevskaya, N. I.; Mukovskii, Y. M.; Mitchell, J.; Ederer, D. L. Mn 3s exchange splitting in mixed-valence manganites. *Phys. Rev. B: Condens. Matter Mater. Phys.* **2002**, *65*, 113102.

(40) Schmid, H. K.; Mader, W. Oxidation states of Mn and Fe in various compound oxide systems. *Micron* **2006**, *37*, 426–432.

(41) Zhang, S.; Livi, K. J. T.; Gaillot, A.-C.; Stone, A. T.; Veblen, D. R. Determination of manganese valence states in (Mn³⁺, Mn⁴⁺) minerals by electron energy-loss spectroscopy. *Am. Mineral.* **2010**, *95*, 1741–1746.

(42) Celorrio, V.; Calvillo, L.; Granozzi, G.; Russell, A. E.; Fermin, D. J. AMnO₃ (A = Sr, La, Ca, Y) Perovskite Oxides as Oxygen Reduction Electrocatalysts. *Top. Catal.* **2018**, *61*, 154–161.

(43) Celorrio, V.; Calvillo, L.; van den Bosch, C. A. M.; Granozzi, G.; Aguadero, A.; Russell, A. E.; Fermin, D. J. Mean Intrinsic Activity of Single Mn Sites at LaMnO₃ Nanoparticles Towards the Oxygen Reduction Reaction. *ChemElectroChem* **2018**, *5*, 3044–3051.

(44) Suntivich, J.; Gasteiger, H. A.; Yabuuchi, N.; Shao-Horn, Y. Electrocatalytic Measurement Methodology of Oxide Catalysts Using a Thin-Film Rotating Disk Electrode. *J. Electrochem. Soc.* **2010**, *157*, B1263.

(45) Shinozaki, K.; Zack, J. W.; Richards, R. M.; Pivovar, B. S.; Kocha, S. S. Oxygen Reduction Reaction Measurements on Platinum

Electrocatalysts Utilizing Rotating Disk Electrode Technique. *J. Electrochem. Soc.* **2015**, *162*, F1144–F1158.

(46) Stoerzinger, K. A.; Lü, W.; Li, C.; Ariando; Venkatesan, T.; Shao-Horn, Y. Highly Active Epitaxial $\text{La}_{1-x}\text{Sr}_x\text{MnO}_3$ Surfaces for the Oxygen Reduction Reaction: Role of Charge Transfer. *J. Phys. Chem. Lett.* **2015**, *6*, 1435–1440.

(47) Risch, M.; Stoerzinger, K. A.; Maruyama, S.; Hong, W. T.; Takeuchi, I.; Shao-Horn, Y. $\text{La}_{0.8}\text{Sr}_{0.2}\text{MnO}_{3-\delta}$ decorated with $\text{Ba}_{0.5}\text{Sr}_{0.5}\text{Co}_{0.8}\text{Fe}_{0.2}\text{O}_{3-\delta}$: a bifunctional surface for oxygen electrocatalysis with enhanced stability and activity. *J. Am. Chem. Soc.* **2014**, *136*, 5229–5232.